

Appendix III: A Tool for Uniform Coating of 300 mm Wafers with Nanoparticles*

A3.1. Introduction

Semiconductor nanoparticles have attracted interest for a wide range of applications that take advantage of the special features that these materials acquire when fabricated into nanoscale structures. At sizes from subnanometer to a few tens of nanometers, quantum mechanical effects alter the optical and electronic properties of the semiconductor, producing quantized energy levels that make them behave as “artificial atoms”[1] or quantum dots whose properties can be tailored by tuning the nanocrystal size. Semiconductor nanocrystals have been used as fluorescent probes in biological imaging and analysis.[2-4] Metal and metal oxide nanoparticles have properties to exploit as catalysts[5-11] and photocatalysts.[12-14] Other proposed applications that take advantage of those special properties of semiconductor nanocrystals include light emitting diodes,[15-18] optical amplifiers[19] and lasers,[20] optically addressed memory,[21] and single-electron transistors.[22]

While applications of nanocrystals that take advantage of quantum size effects have received considerable attention, device fabrication remains a significant challenge

* This work was completed with Dean Holunga, who is a co-author.

due to difficulties of controlling nanocrystal size and placement, particularly with materials that are compatible with today's device fabrication infrastructure. Preventing process and tool contamination remains a major challenge when exotic materials or colloidal synthesis are considered, even though colloidal nanoparticles have been synthesized with precise control of size and optical properties for a wide range of materials, including silicon.[23-26]

Nevertheless, nanoparticle-based microelectronic devices have been fabricated without adverse effects on processing tools, albeit for less exotic applications. Tiwari and co-workers[27] proposed a silicon nanocrystal based memory to overcome the charge leakage that plagues conventional floating gate devices as they are scaled into the sub-100 nm size regime. Both devices are metal oxide semiconductor field effect transistor (MOSFET) structures that incorporate a floating gate to store charge. In the conventional device, the floating gate is a continuous semiconductor layer that is separated from the silicon substrate by a thin barrier tunnel oxide. To store or erase information, charge is induced to tunnel through an oxide layer into the floating gate. Unfortunately, any leakage path between the floating gate and the underlying channel will eventually dissipate all the stored charge. Tiwari's floating gate of isolated nanocrystals reduces the probability of complete information (charge) loss by separating the floating gate into a number of isolated storage elements within each transistor. The devices were fabricated by spontaneous decomposition during chemical vapor deposition. Feng, et al.[28] have produced nanocrystals in the floating gate by thermal annealing after ion implantation. Neither method affords direct control over the particle size distribution. Moreover, at least in the case of ion implantation, *in situ* nucleation leads to a distribution of

nanocrystals through the depth of the gate oxide.[29] The resulting variability in the nanocrystal-to-channel spacing leads to a distribution in leakage current over the area of the transistor. Ion implantation leads to a distribution of nanoparticle sizes at different depths,[29] presenting a challenge in obtaining a uniform tunneling distance between the gate and the nanocrystal.

Ostraat[30] demonstrated an alternate approach to creating a nanocrystal floating gate MOSFET. Silicon nanoparticles were produced as an aerosol by gas-phase thermal decomposition of silane. The silicon nanoparticles were then oxide passivated while still suspended in the carrier gas. The oxide layer was created on the aerosol nanoparticles in two ways: (1) by chemical vapor deposition of tetraethylorthosilicate (TEOS), or (2) by high temperature oxidation (HTO) of the surface of the aerosol silicon nanoparticles. After oxide passivation, the core/shell nanoparticles were deposited by thermophoretic diffusion onto a previously prepared tunnel-barrier oxide on 200 mm diameter silicon wafers. The HTO-passivated nanoparticles met the stringent contaminant limits and were processed to produce high performance devices through an industrial fabrication facility.[31]

Although the devices produced by Ostraat, et al. showed excellent performance characteristics and demonstrated that aerosol-synthesized silicon nanocrystals can safely be taken through conventional device lithography and etching processes, many aspects of the synthesis require further development before such processes see commercial applications. Foremost is discomfort of tool owners with taking particle laden wafers into the fabrication facilities, a problem that will require addressing a number of real and imagined hazards to the process equipment. Questions about the entrainment of

nanoparticles from wafer surfaces[32-36] and, especially, about the existence of agglomerates that might more easily detach can only be addressed once suitable nanoparticle-coated wafer samples can routinely be processed for testing.

The original nanoparticle synthesis employed a low-throughput, multistage laminar flow aerosol reactor that enabled precise control of the size and structures of the product nanoparticles, but that produced relatively low number concentrations, $1 * 10^6$ to $3 * 10^6 \text{ cm}^{-3}$, in 1500 sccm carrier gas flow rates. Nanoparticle coverage of a 200 mm wafer, dense at the center and sparse near the edge, required from 4 to 12 hours for each wafer, far too long for a production process. Extension to similar coverage of the 300 mm wafers would, at a minimum, double this deposition time.

Numerous groups have demonstrated much higher nanoparticle synthesis rates than that of Ostraat. Flame synthesis[37-40] reactors produce hundreds of grams per hour in the laboratory, and kilograms or more in industrial reactors, but are not suitable for the materials of interest here. Laser-induced decomposition[41-43] and plasma synthesis[44-45] can produce large quantities of silicon or other non-oxide nanoparticles, but the precise control of the state of agglomeration achieved by Ostraat, et al. remains a challenge. Recently, Holunga[46] et al. demonstrated a higher throughput multistage reactor that employs turbulent mixing and short residence times to improve on the particle properties achieved in the laminar flow aerosol reactor. The short residence time allows number concentrations as high as 10^9 cm^{-3} to be processed with minimal agglomeration. The resulting heterogeneous core/shell Si-SiO₂ aerosol nanoparticles provide an enabling technology for accelerated nanoparticle device processing.

While the deposition chamber used in early aerosol nanoparticle device synthesis demonstrated the potential of the approach, the areal density of deposited nanoparticles varied significantly over the surface of the wafers. While this proved useful in initial studies of device properties by enabling a range of devices to be produced in a single experiment, production tools will have to produce deposits that are uniform over the entire surface of larger (300 mm) production wafers.

The present chapter focuses on the latter challenge. The discussion that follows reports on the design and characterization of a nanoparticle deposition tool for coating of 300 mm silicon wafers with aerosol synthesized core/shell nanoparticles produced using the multistage turbulent mixing aerosol reactor.

A3.2. Design

The deposition chamber, illustrated schematically in figure A3.1, consists of two radially mounted parallel plate heating and cooling surfaces. The aerosol is introduced and removed orthogonally through 1/2" OD SS tubing at the center of the wafer. Three concentric heat sources provide a nearly uniform heat flux to the top plate. The bottom plate is cooled using a heat transfer fluid.

For radially outward, isothermal flow of a Newtonian fluid between flat plates, and in the creeping flow limit, the velocity profile as a function of z (height) and r (radius) is[47]

$$v_r(r, z) = \frac{3Q}{4\pi r Z} \left(1 - \left(\frac{z}{Z} \right)^2 \right), \quad (\text{A3.1})$$

where Q is the volumetric flow rate, z is the normal distance from the midplane between the plates, and Z is half the distance between the plates. This profile remains only

approximately valid if a small temperature gradient exists between surfaces; however, for a small ΔT at relatively large absolute T , the important characteristic remains that the velocity in the radial direction decreases as r^{-1} .

The thermophoretic velocity for ultrafine particles, v_{th} , can be described as[48]

$$v_{th} = -Th \frac{\mu}{\rho T} \frac{\partial T}{\partial z}, \quad (A3.2)$$

where ρ is the density, μ is the viscosity of the effluent gas, T is the absolute temperature, and z is the coordinate of directional movement. The dimensionless number, Th , has been experimentally determined to be about 0.5.[49] If the absolute temperature is relatively high enough and the temperature gradient remains similar between the plates at all radial positions, then the z-axis thermophoretic velocity is nearly constant throughout the chamber.

The surface area being covered increases as the flow expands radially outward from the center of the wafer.

$$\frac{\partial A}{\partial r} = 2\pi r = C(r). \quad (A3.3)$$

Since the deposition rate needed is proportional to both $v_{avg}(r)$ and $C(r)$, while the velocity of the feed particles is decreasing with r^{-1} , any r dependency in deposition can be eliminated using radial geometry. Ignoring Brownian diffusion, a constant deposition velocity from the z direction should yield a homogeneous deposition flux at all locations on the wafer. With a robust design allowing flexibility in adjusting flow rates and temperature gradient, a suitable operating condition can be reached that would yield uniform deposition.

The critical feature for this deposition chamber is ensuring non-separating laminar flow through the nozzle and preventing re-circulating flow. Aerosol in recirculation zones may agglomerate and either deposit on the chamber walls or re-enter the deposition flow and be driven to the collection surface in a non-desired size and configuration.

The nozzle shape was determined using a potential flow argument, in rectilinear coordinates, for stagnation flow around a corner. This approximation is locally valid as the nozzle begins to bend since the boundary layer is developing through the radius of the bend and also outward from the stagnation point above the wafer, approximating open channel non-viscous flow. In physical terms, the combination of a larger diameter inlet tubing, a small power-law hyperbolic nozzle (small change in r) and a narrow gap allowed the flow field to be approximated in rectilinear coordinates. The classical fluid flow field for an open channel incompressible laminar flow field around an L-shaped corner can be described by the vector equation,

$$\hat{v} = Ax\hat{i} - Ay\hat{j}, \quad (\text{A3.4})$$

where x and z are the coordinates and A is an arbitrary constant dependent on the volumetric flow rate within the dimensions of the structure. The flow field solution is a hyperbolic family of streamlines, $\varphi = xy$, wherein the channel width w (from the y -axis) is identical to channel height h from the x -axis. By symmetry, a point on a curve at $\varphi(a, b)$ is also on the same streamline at $\varphi(b, a)$. Each streamline acts as a "pressure" wall to the fluid on either side of the streamline. A physical wall could be inserted without altering the stream function. The stream function for non-equal channels, $w \neq h$, is such that a fluid element entering at (wx_o, hy_o) might be constrained to find the point (wy_o, hx_o) on the way out. If so, the vector flow field above is transformed,

$$\hat{v} = Awxi\hat{i} - Ahyj\hat{j} . \quad (\text{A3.5})$$

Using the stream function approach with,

$$-\frac{\partial\varphi}{\partial x} = v_y = -Awy , \quad (\text{A3.6})$$

$$\frac{\partial\varphi}{\partial y} = v_x = -Ahx , \quad (\text{A3.7})$$

yields the separable differential equation,

$$\frac{\partial y}{\partial x} = \frac{wy}{hx} , \quad (\text{A3.8})$$

and a solution of the form,

$$xy^{-\frac{h}{w}} = \text{Constant} , \quad (\text{A3.9})$$

which describes a family of power law hyperbolic-type streamlines. A properly chosen streamline can be used to form the equation for the nozzle curve, with the nozzle shape described as

$$\varphi = \varphi_0 = (x - x_0)(y - y_0)^{-\frac{h}{w}} , \quad (10)$$

provided that dynamical pressure inequalities do not lead to flow separation. This stipulation simply requires that the maximum flow velocity be essentially unchanged through the bend as the fluid leaves the nozzle and begins to traverse the deposition surface.

In two-dimension axisymmetric flow, i.e., cylindrical coordinates, the stream function solution to stagnation flow[49] from a jet is $\text{Constant} = r^2z$. In the chamber, the actual ratio of w/h is 2.65. Applying the offset, (x_0, y_0) to the rectilinear solution,

effectively chose a streamline very close to the axes (small r) in which the error in the exponent became negligible.

This curve chosen should also smoothly join with the inlet tubing wall and the top plate of the chamber and be symmetric in the azimuthal. When the maximum flow velocity through the nozzle is similar to the maximum flow velocity of the gas in the inlet tubing, the dynamical pressure varies little, and streamlines remain intact. Acceleration or deceleration of gas through this region would give rise to pressure boundaries beyond which recirculation zones could appear. Particles trapped in recirculation pockets will agglomerate and eventually settle out, preventing homogenous coverage of a surface with particles of equivalent size.

The heater/chamber was modeled in Fluent using a laminar flow two dimension axisymmetric solver. The dimensions of an actual MDC flange were used in creating the model chamber. Incoming aerosol flow, 1500 sccm, was provided an entrance length sufficient to develop a parabolic velocity profile. The top flange was heated with ring-heaters that were assumed to be able to provide a constant heat flux, figure A3.1, or constant temperature, and the water coolant (which would have turbulent flow) was assumed to have heat removal capacity such that the metal in contact with the coolant was only 5–10 K above the incoming water temperature. A 3D $\kappa - \epsilon$ turbulent model for the cooling water limits was also modeled, figure A3.2, wherein 30 LPM of water at 300 K is diverted into two opposing tangentially outward jets to cool 1800 W of energy transferred to the outer surface. The heat transfer coefficient for the top surface included conduction through a zone corresponding to the stainless steel MDC flanges as well as

convection into a laminar flow gas. The modeled temperature rise of the coolant is less than 10 K.

With a working nozzle geometry determined, the Fluent model was run using a constant flux (power) source for the heaters rather than a constant temperature boundary condition. The necessary conditions of nearly uniform temperature gradient and adequate heat removal were also met in this scenario.

At a concentration of 10^9 cm^{-3} monodisperse 10 nm aerosol nanoparticles have a characteristic agglomeration time constant of $\tau_a \sim 1 \text{ s}$. The chamber operation must be robust enough to allow for higher flow rates of diluted nanoparticles should agglomeration need to be suppressed during the deposition process. Figures A3.3–A3.4 shows modeled velocity profiles of 1500 sccm, 15,000 sccm, 30,000 sccm, and 60,000 sccm. The modeling indicates that flow rates up to 15,000 sccm are possible when employing a 2 mm gap between the wafer and heated top plate.

Wafer curvature is commonly seen in large wafers exposed to thermal gradients such as those found in plasma etch processes. The potential of having wafer curvature arising from the axial variation in thermal expansion was briefly investigated. Assuming isotropic expansion, a constant thermal expansion coefficient of $\sim 4 * 10^{-6} \text{ K}^{-1}$, an axial temperature change of 1 K (about 5 times larger than modeled predictions) through a 50 μm wafer, the predicted radius of curvature of in a 300 mm wafer is $\sim 125 \text{ m}$. The predicted variation in height from center to edge is less than 0.1 mm. Although the curvature is minimal in this apparatus, the variation in height scales linearly with the temperature drop. Thus, wafer curvature may have a significant effect on deposition

patterns at larger temperature gradients. Greater deposition nearer the edges would be expected as the flow slows at a rate greater than r^{-1} .

A3.3. Experimental Apparatus and Methods

Oxide-coated silicon nanocrystals are produced in a turbulent mixing aerosol reactor described previously.[46, 50] A fraction of the stream is monitored continuously by a radial differential mobility analyzer[51-55] (RDMA) and a fA-resolution electrometer. The remainder of the 8–12 nm particle stream, with a concentration of $\sim 10^8 \text{ cm}^{-3}$ and $\sigma_g \approx 1.1$, is sent via 1/4" stainless steel tubing to the deposition chamber inlet.

The deposition chamber consists of two modified MDC 18" stainless steel vacuum flanges that serve as radially mounted parallel plate heating and cooling surfaces. The aerosol is introduced orthogonally through 1/2" O. D. stainless steel tubing above the top plate at the wafer center and removed orthogonally at the wafer center from below through the bottom plate. Two concentric ring heaters and a third side-mounted band heater with a concentric ring-connected mount provide a nearly uniform heat flux to the top plate. A hollowed annulus in the bottom plate allows for heat transfer through the flange to a cooling fluid. Re-circulated cooled water at 293 K at a flow rate of 30 LPM cools the bottom flange. The coolant is sealed using a stainless steel covering plate with a Viton O-ring gasket. A small bi-directional nozzle is employed to provide equal coolant fluid flow around either perimeter of the water jacket. A single drain is located radially opposite the coolant source. A flat Viton gasket separates the two flanges, serving as a thermal resistor to provide a more uniform temperature profile between the flanges.

The top plate is supported by three stainless steel legs. The bottom plate rests on a stainless steel jack that is manually raised and lowered during loading/unloading operations. All stainless steel surfaces are electropolished.

To maintain a uniform top plate temperature, each heating element is powered through a Eurotherm 7100A thyristor monitored with thermocouples and PID controllers. The temperature profile and streamlines from a two-dimension axisymmetric solver in Fluent are shown in figures A3.5–A3.6. A flow rate of 1500 sccm was used. The temperature drop from top plate to the wafer remains relatively uniform across the entire deposition region from the center, figure A3.5A, to the edge of the wafer, figure A3.5B. However, to avoid a region of sparse deposition from a reverse temperature gradient, observed in the modeling, when the aerosol is introduced relatively cold, a heating tape, thermocouple, and PID assembly are used to preheat the inlet aerosol.

Figure 6 shows the corresponding streamlines for 1500 sccm flow to the modeled temperature profiles shown previously. Streamlines are parallel through the nozzle bend, figure A3.6A, and over the wafer surface. Beyond the edge of the wafer, from the geometry imposed using this particular size of MDC flanges, figure A3.6B, a recirculation pocket exists. However, this should have no effect on particle deposition over the wafer substrate.

Wafers are loaded using quartz-sleeved stainless steel forks and rest upon three quartz or Teflon pegs in the chamber, providing a uniform wafer to plate distance and preventing contact with metal surfaces. The wafer is physically situated 2 mm below the heated top plate. With the absolute temperature relatively high, and the temperature gradient relatively large and uniform, small radial variations in temperature have little

effect on thermophoretic transport. The quartz/Teflon pegs sit in machined depressions and the pegs are removable and replaceable. The adjustable height of the wafer adds another degree of freedom in determining thermophoretic velocity.

AFM samples were drawn from a center strip of a 150 mm [100] Si wafer that was tiled into 14 squares sized 1 cm x 1 cm using a wafer saw or cut into similar sized pieces using a diamond-tipped scribe. Before deposition, the tiled pieces were cleaned by sonication in methanol, rinsed in deionized water, and dried using a jet flow of nitrogen. The tiled wafer was reconstructed on an intact wafer in the chamber, with the two “halfmoon” pieces secured using stainless steel clips.

All stainless steel surfaces were electropolished and cleaned with methanol prior to use within the cleanroom environment.

Non-contact AFM images were acquired over 512 x 512 resolution from a 5 μm x 5 μm grid. The AFM tip was estimated to be ~ 30 nm in diameter. Particle counts over the entire grid to determine coverage are reported in figure A3.12B and represent ~ 2000 particles per image.

A3.4. Results

Additional modeling of particle transport was conducted using Femlab. The results are shown in figures A3.7–A3.10. The model used was a laminar flow, two-dimension axisymmetric representation of the deposition chamber. Temperature boundary conditions were imposed based on the results obtained earlier using Fluent, creating a temperature drop of ~ 30 K between the heated chamber top and the wafer. For simplicity, the particles are treated as a continuum species with uniform inlet concentration and temperature. The particles are subject to convection and

thermophoresis as they travel through the chamber. Brownian diffusion is imposed for a single mode particle size, 10 nm, but particle loss to walls other than the wafer surface is neglected.

Figure A3.7 shows the particle distribution in the chamber with uniform top and bottom temperature, $\Delta T = 165$ K, and the incoming aerosol-laden N_2 15 K cooler than the chamber top. Figures A3.8–A3.10 show results for increasing flow ratios. A flow rate of 1600 sccm leads to insufficient deposition on the outer edge of a 300 mm wafer, but would be sufficient for a 150 mm wafer. The arrows in the figures indicate thermophoretic flux, $v_{th}c$, and that uniform deposition is predicted over the central portion of the wafer. Increasing the flow rate to 3600 sccm results in uniform deposition on a 300 mm wafer, figure A3.10, but is only achieved when some particles bypass deposition. At intermediate flow rates, uniform deposition coverage extends outward with increasing flow rate, while deposition rate decreases for similar aerosol inlet concentration. figure A3.11 summarizes these model observations. Near $r = 1$ mm, each trace predicts some inconsistency in the deposition uniformity. This perturbation could be reduced in the model, similar to that observed in the 3600 sccm trace, by adjusting the inlet temperature a few degrees lower, depending on the flow rate.

To examine the deposition uniformity attained by the deposition tool, silicon nanoparticles were deposited on a 150 mm wafer for 80 min with an aerosol flow rate of 1600 sccm and an aerosol concentration of $2 * 10^8 \text{ cm}^{-3}$. As seen in the images in figure A3.13, the coverage was kept well below the monolayer than would be sought in device fabrication to facilitate quantitative areal density measurements. The particle size distribution of this test aerosol is shown in figure A3.12A. The major mode in the

distribution was 8.5 nm. The minor second mode at ~11 nm reveals that limited (~10%) aggregation occurred between the outlet of the synthesis reactor and the RDMA. The areal density of the deposited particles, shown in figure A3.12B, is quite uniform, varying less than $\pm 5.5\%$ over the radial and azimuthal by distributed samples probed.

Modeling in Fluent indicated that the particle stream needed to be preheated to a temperature within ~ 20 K of the hot plate temperature to achieve deposition uniformity at the wafer center. A temperature too high produced a correspondingly larger thermal gradient near the center and the modeled deposition rate exceeded that of the outer surface. If too cool, figure A3.14, then the model predicts insufficient or no deposition at the center. Heat transfer within the silicon wafer is faster than through the aerosol-containing N_2 , raising the temperature of the wafer center above that of the heated inlet stream, and driving particles away from the wafer.

The reversed temperature gradient was also predicted with modeling in Femlab, as seen in figures A3.15–A3.16. The magnitude of the thermophoretic flux away from the wafer is several times that of the flux toward the surface, indicating that the reversed temperature gradient is much greater.

A3.5. Conclusions

A 300 mm capable laminar flow thermophoretic deposition device demonstrates near uniform coverage of nanoparticles on a 150 mm wafer. Modeling suggests device operation is robust over a wide range of flow rates. A sparse array of particles randomly oriented over the surface was stably attached and remained adhered over a two-month period in which characterization by AFM was performed. Longer deposition times are expected to maintain deposition uniformity and yield coverage approaching monolayer.

Deposition of nearly monodisperse nanoparticles may also self-assemble into close-packed structures, provided that agglomeration in the aerosol phase is avoided. Device fabrication with aerosol nanoparticles deposited using thermophoresis remains a potential new process for meeting narrower bandwidth requirements or producing new devices in which the nanoparticles' spatial positioning must meet tight tolerances.

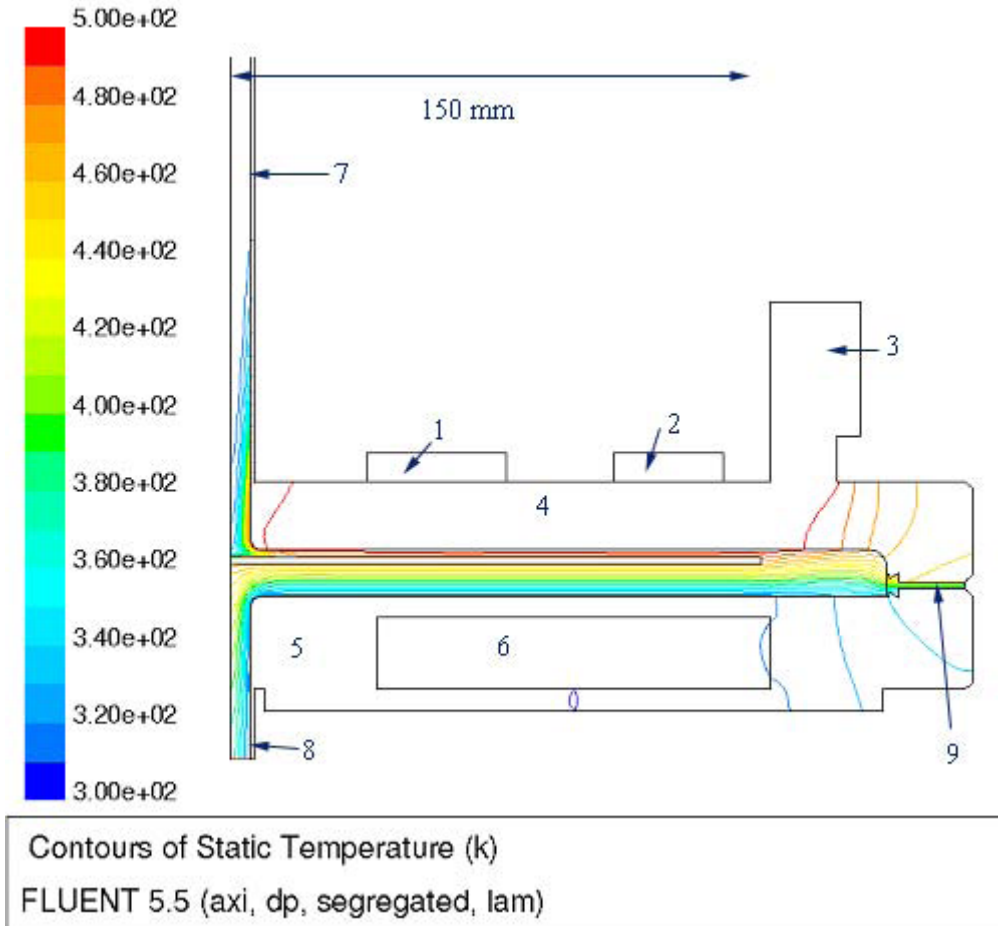


Figure A3.1. Schematic of Thermophoretic Depositor with Isotherms.

Isotherms of deposition chamber modeled in Fluent. Components of chamber: 1. Inner ring heater. 2. Outer ring heater. 3. Band heater and mount. 4. Top MDC stainless steel Flange. 5. Bottom MDC stainless steel Flange. 6. Water cooling chamber. 7. Aerosol inlet. 8. Gas outlet. 9. Viton Gasket. Modeled average current supplied to the heaters (with listed power capacity) as follows: 1. Inner ring heater, 0.4 A/1000 W, middle ring heater, 2. 0.6 A/1500 W, 3. Outer band heater 7.5 A/1500 W.

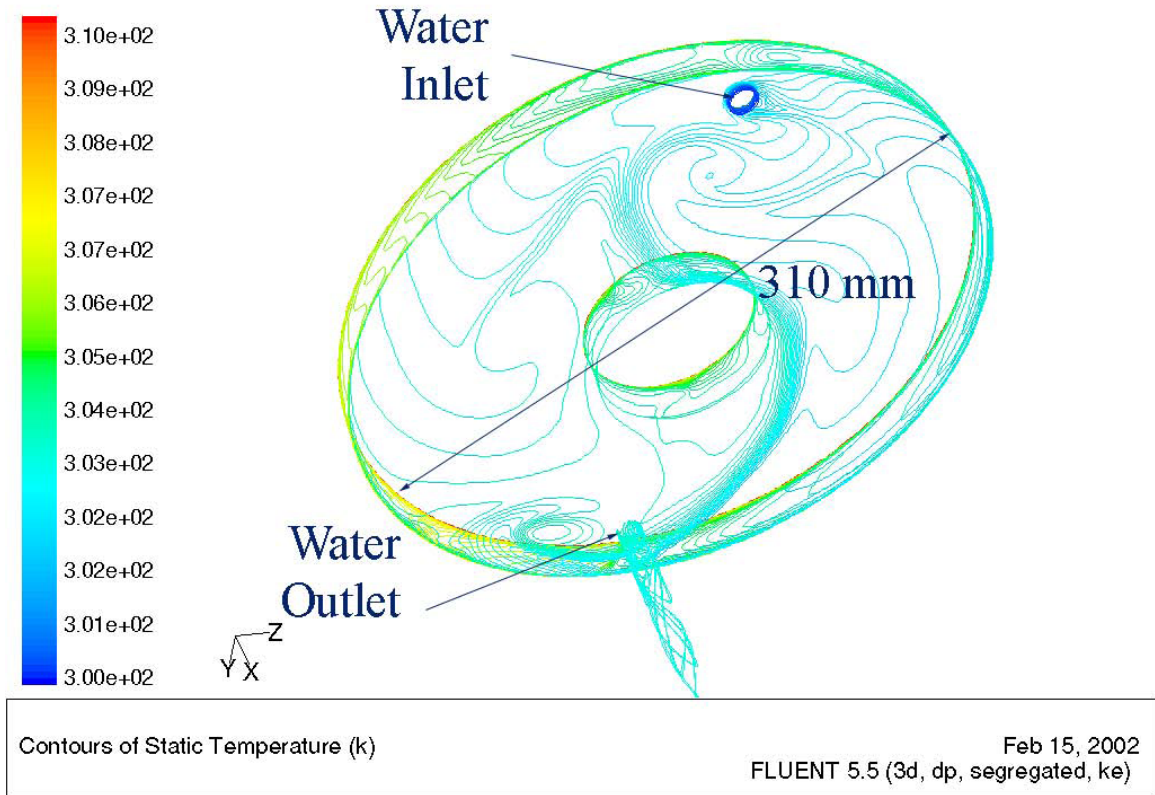


Figure A3.2. Modeled Temperature Profile.

Modeled temperature rise for a constant 1800 W heater on the outer band and top of a water-cooled chamber with 30 LPM flow rate.

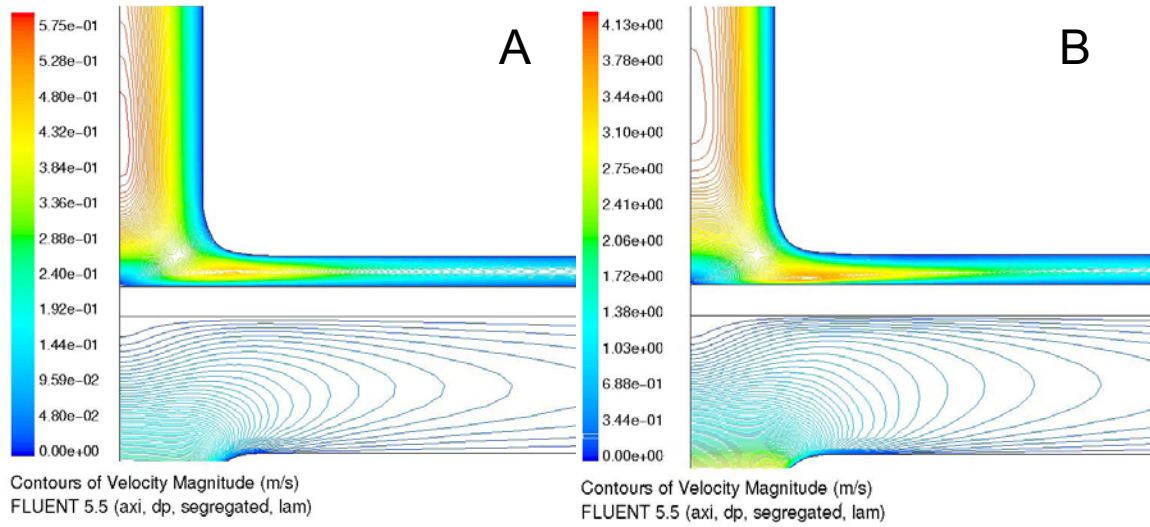


Figure A3.3. Modeled Velocity Contours for Flow Rates of 1.5 and 15 SLM.

Velocity contour plots for flow rates (A) 1500 sccm and (B) 15,000 sccm without separation as modeled in Fluent.

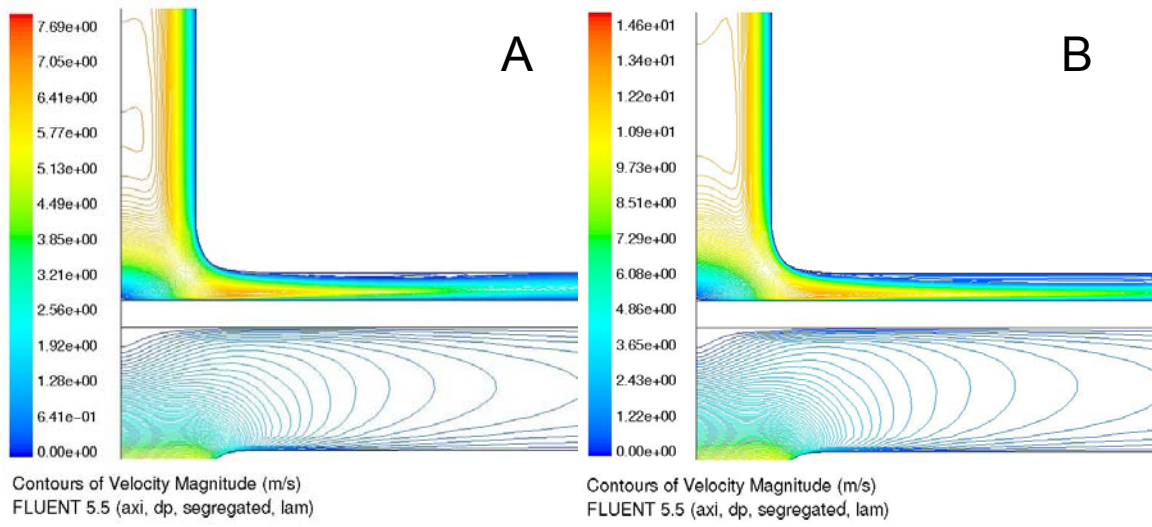


Figure A3.4. Modeled Velocity Contours for Flow Rates of 35 and 60 SLM.

Velocity contour plots for flow rates of (a) 35,000 sccm (b) 60,000 sccm with separation as modeled in Fluent.

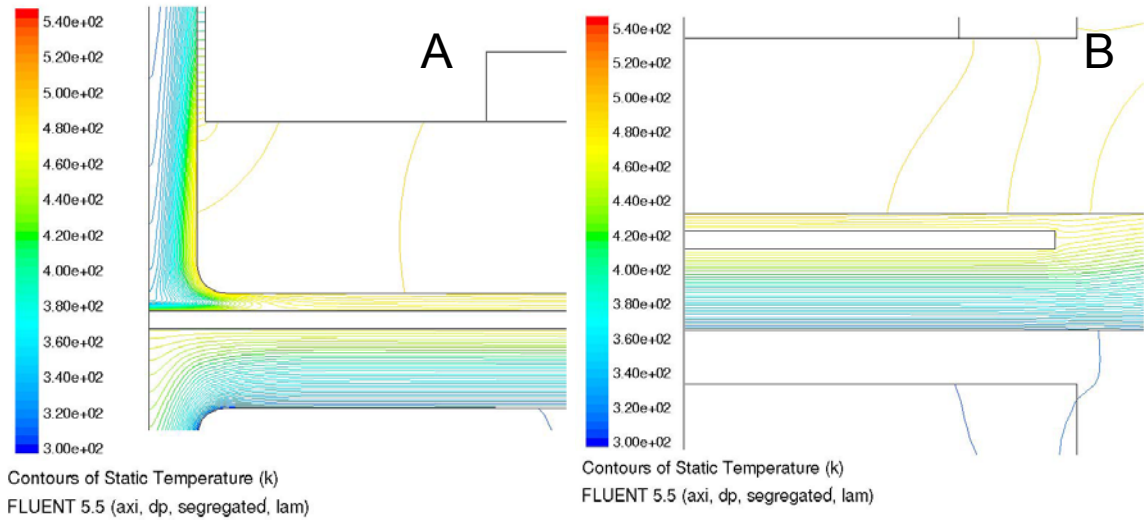


Figure A3.5. Modeled Temperature Contours.

Temperature contour plots modeled in Fluent. (A) Modeled temperature profile at the inlet and outlet region. (B) Modeled temperature profile at the edge of wafer region.

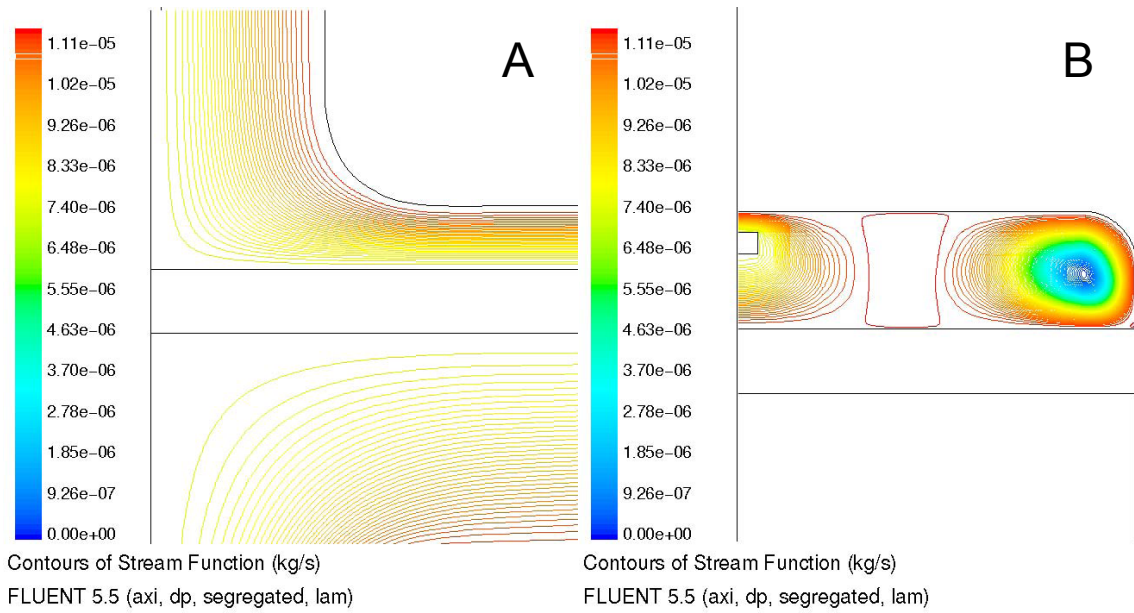


Figure A3.6. Modeled Stream Function Plots.

Stream function plots modeled in Fluent for flow rates of 1500 scfm. (A) Modeled streamlines at the inlet and outlet region. (B) Modeled streamlines at the edge of wafer region.

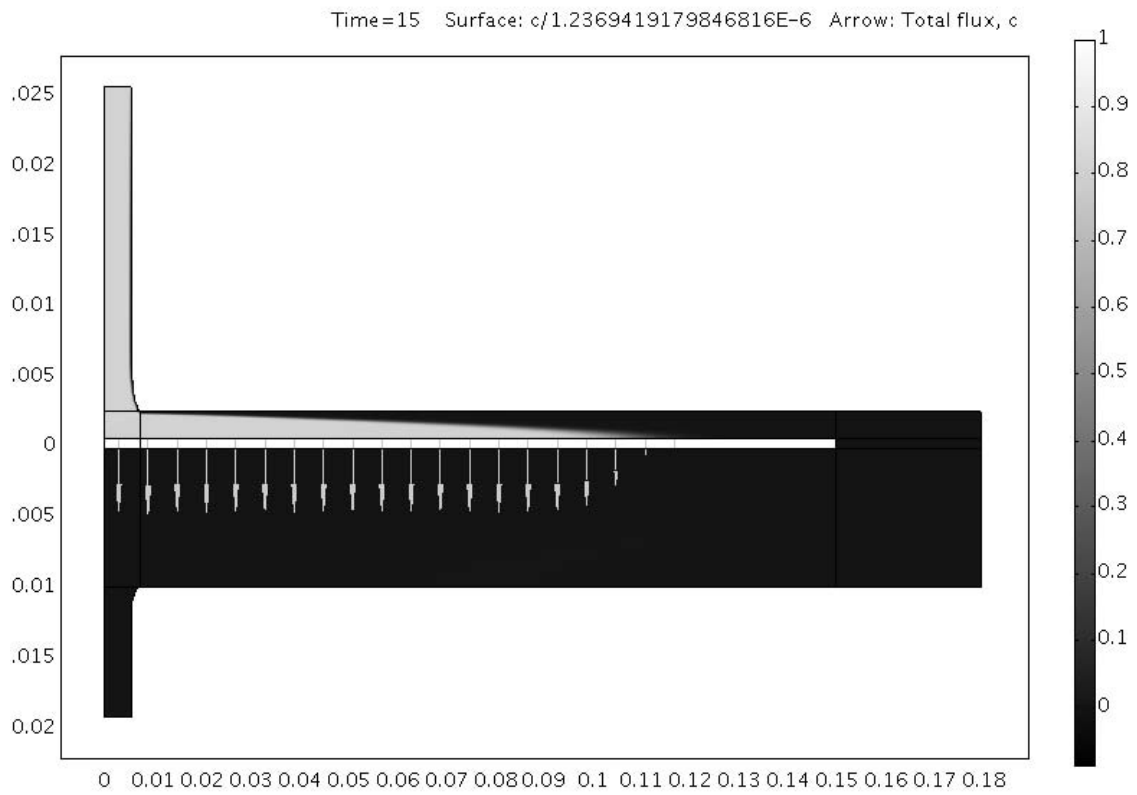


Figure A3.7. Modeled Deposition Profile.

Normalized particle deposition and concentration at 1600 sccm modeled in Femlab.

Arrows indicate particle flux rate at the wafer surface.

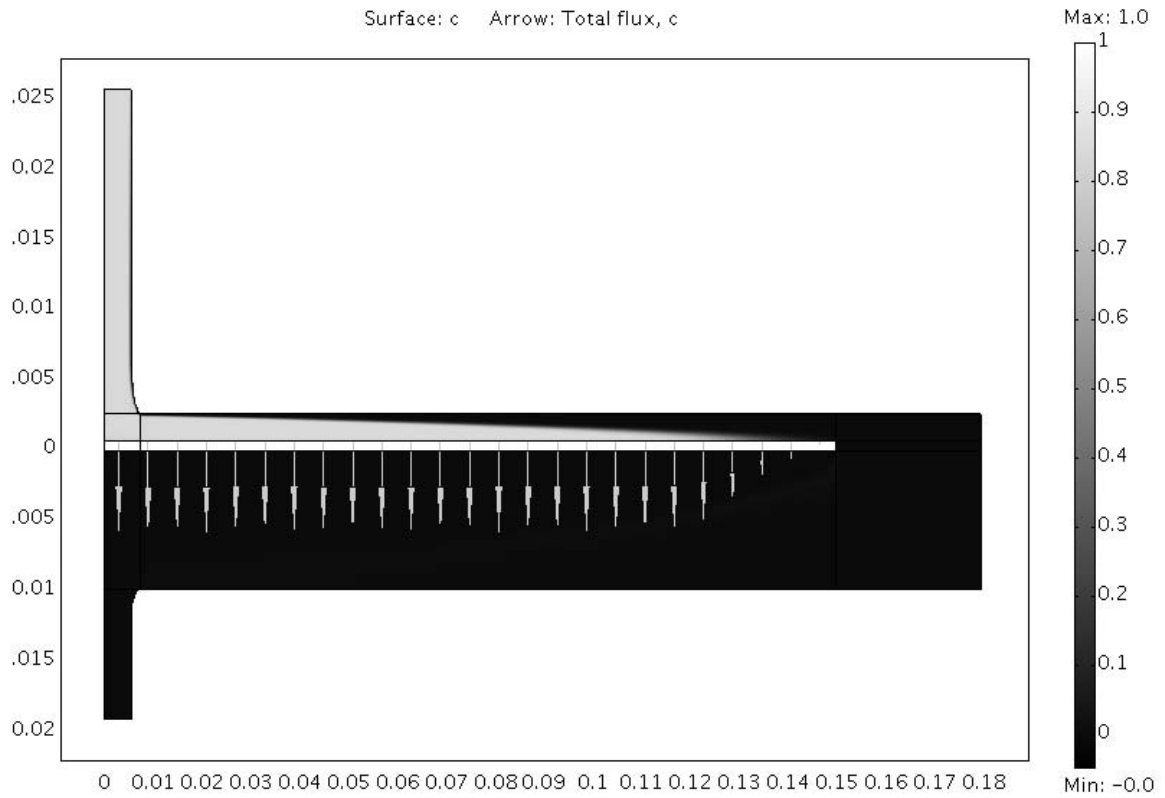


Figure A3.8. Modeled Deposition Profile.

Normalized particle deposition and concentration at 2400 sccm modeled in Femlab.

Arrows indicate particle flux rate at the wafer surface.

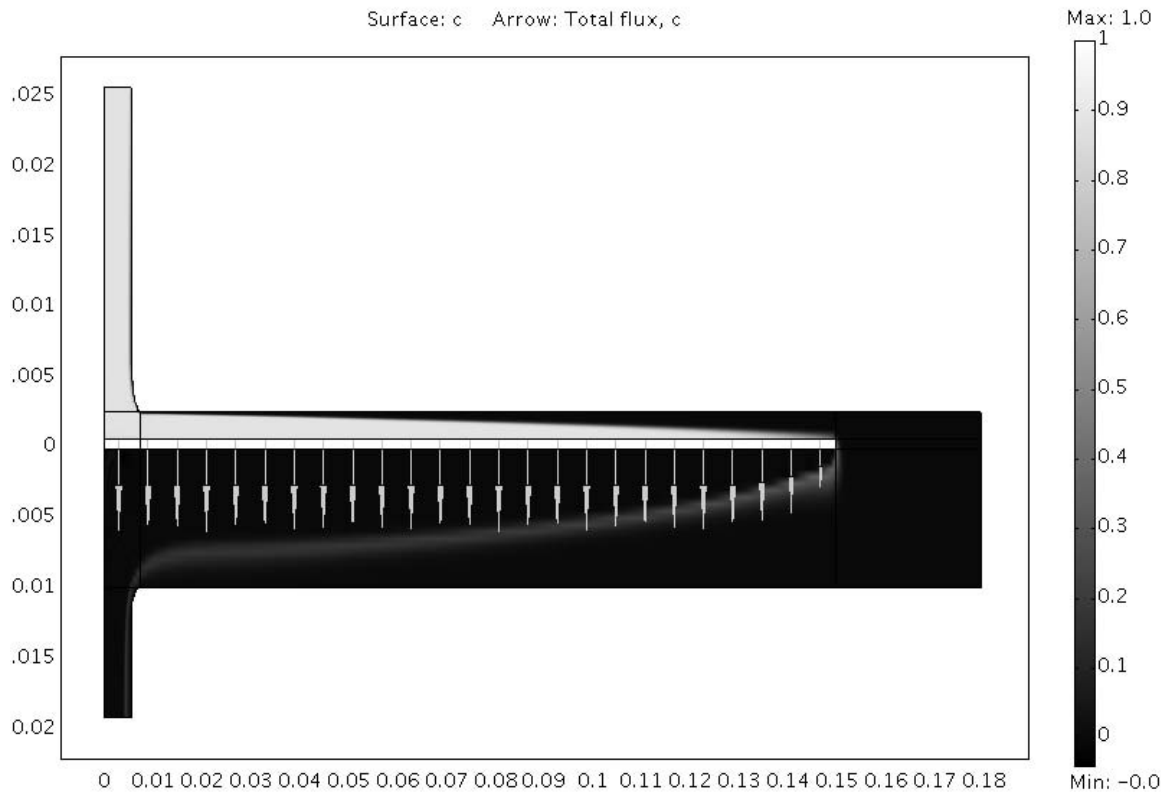


Figure A3.9. Modeled Deposition Profile.

Normalized particle deposition and concentration at 3000 sccm modeled in Femlab.

Arrows indicate particle flux rate at the wafer surface.

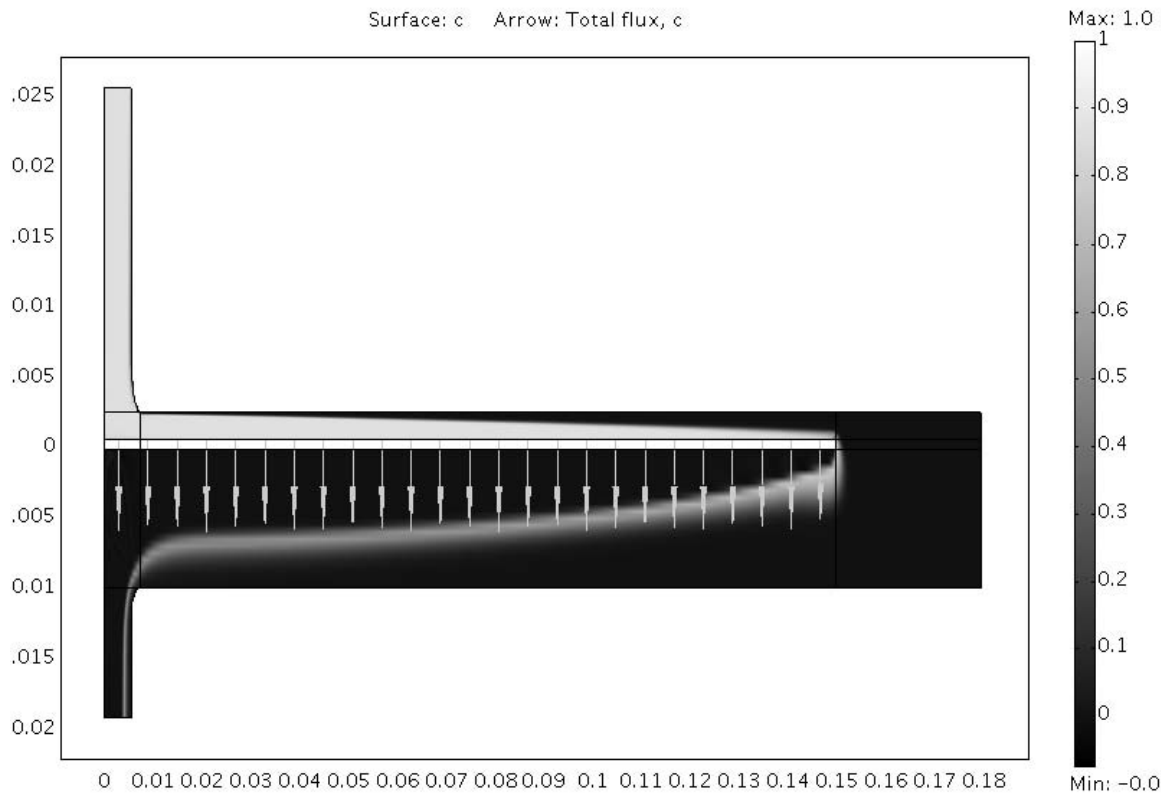


Figure A3.10. Modeled Deposition Profile.

Normalized particle deposition and concentration at 3600 sccm modeled in Femlab.

Arrows indicate particle flux rate at the wafer surface.

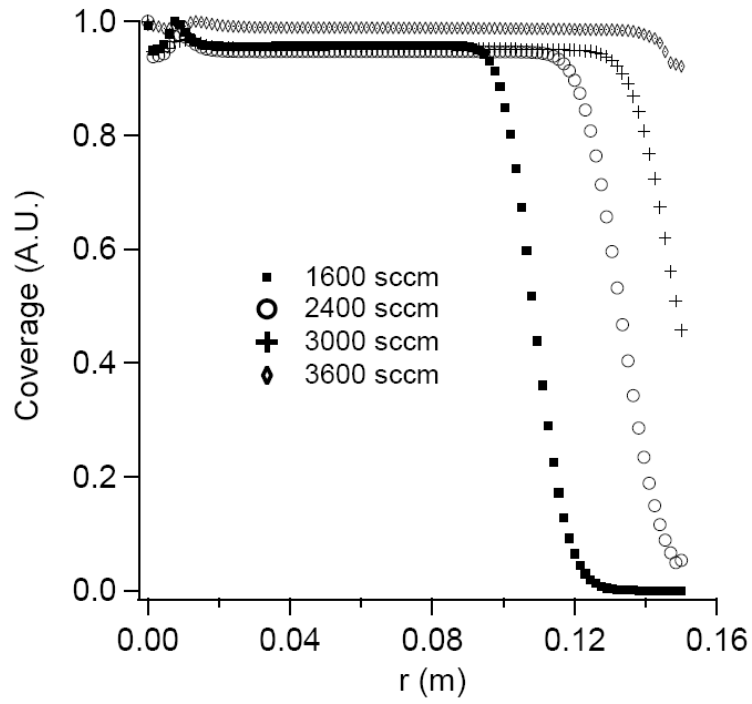


Figure A3.11. Plot of Deposition Profile.

Model predictions for particle deposition on 300 mm silicon wafer at various flow rates.

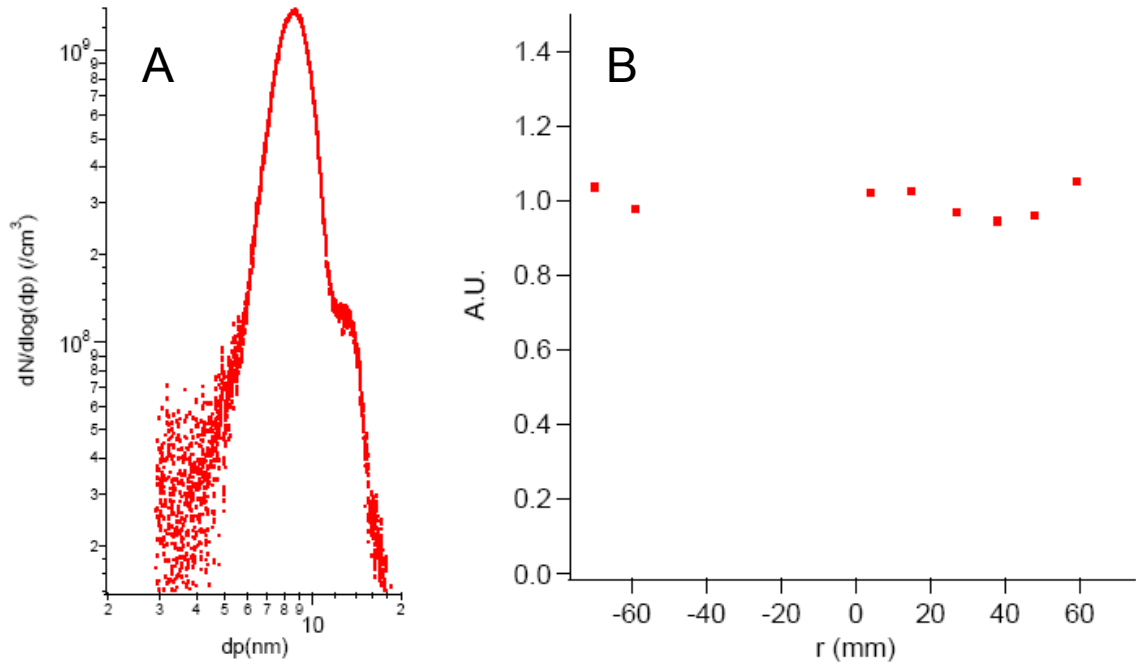


Figure A3.12. Particle Size Distribution and Wafer Coverage.

PSD and particle coverage on 150 mm silicon wafer. AFM images are seen in Figure A3.13. (A) PSD of nanoparticles deposited on 150 mm wafer. (B) Particle coverage normalized by mean.

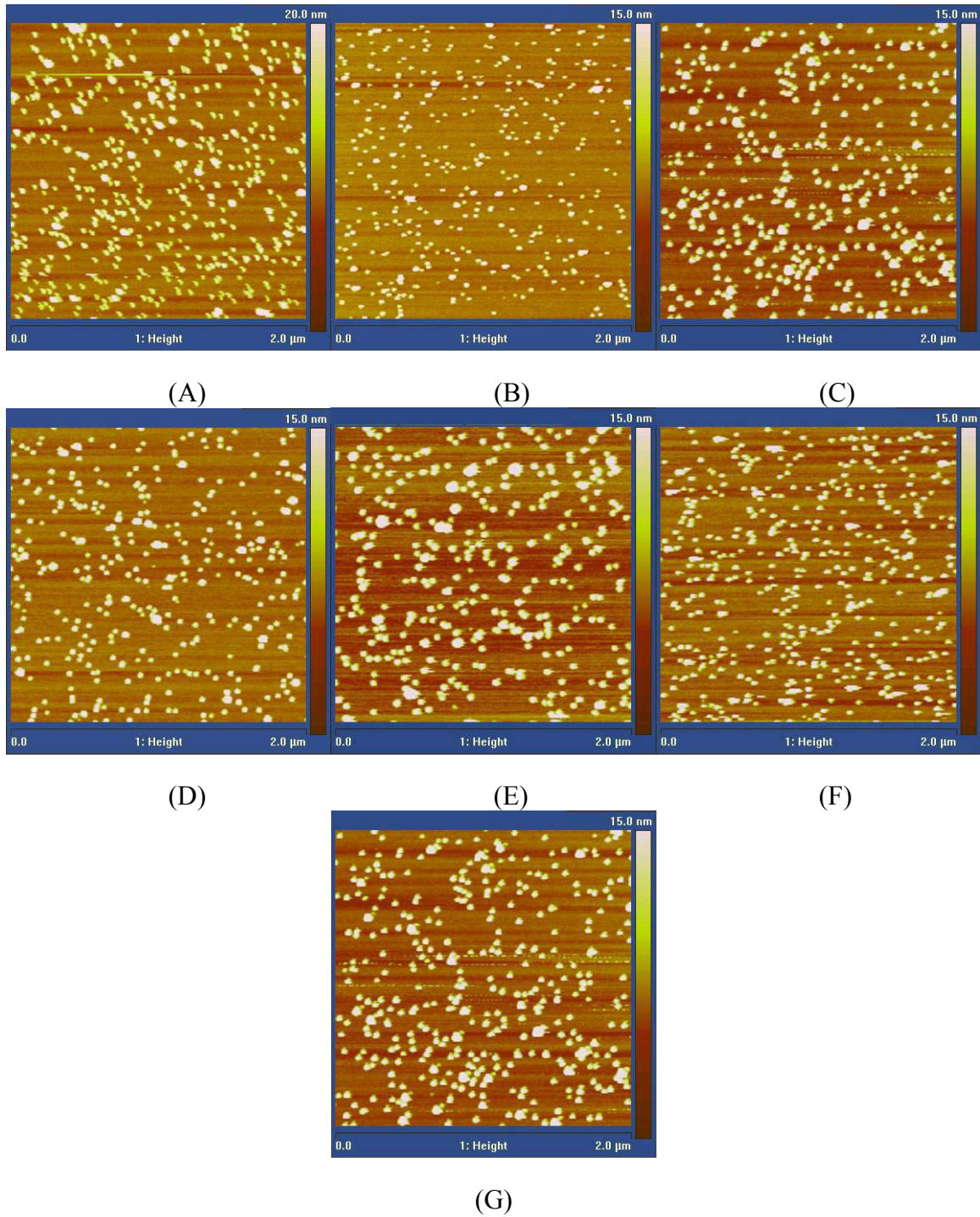


Figure A3.13. AFM Images of Deposited Particles.

AFM images of particle deposition on 150 mm wafer. (A) $r = 70$ mm, (B) $r = 59$ mm, (C) $r = 48$ mm, (D) $r = 38$ mm, (E) $r = 27$ mm, (F) $r = 15$ mm, (G) $r = 4$ mm.

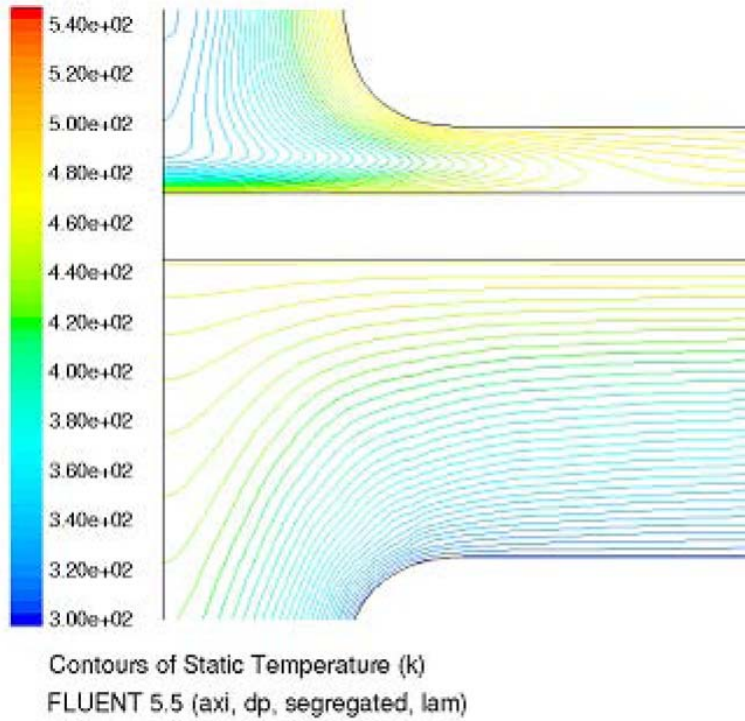


Figure A3.14. Modeled Inlet Temperature Distribution without Inlet Heating.

Model predicts an unfavorable temperature gradient at the wafer surface when the aerosol is not preheated.

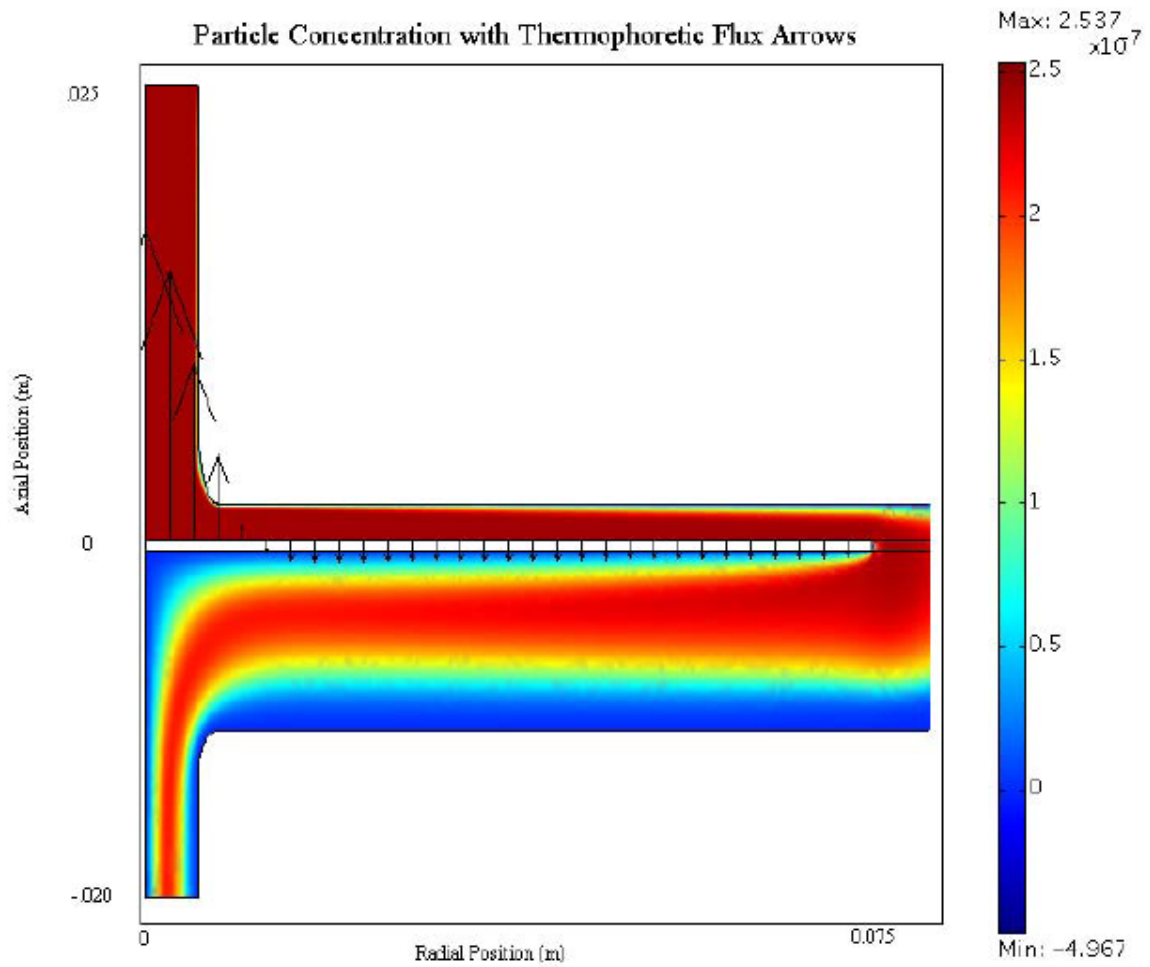


Figure A3.15. Deposition Profile without Inlet Heating.

Model predicts the lack of deposition at the wafer center if the aerosol is not preheated.

The arrows are proportional to the magnitude of thermophoretic particle flux.

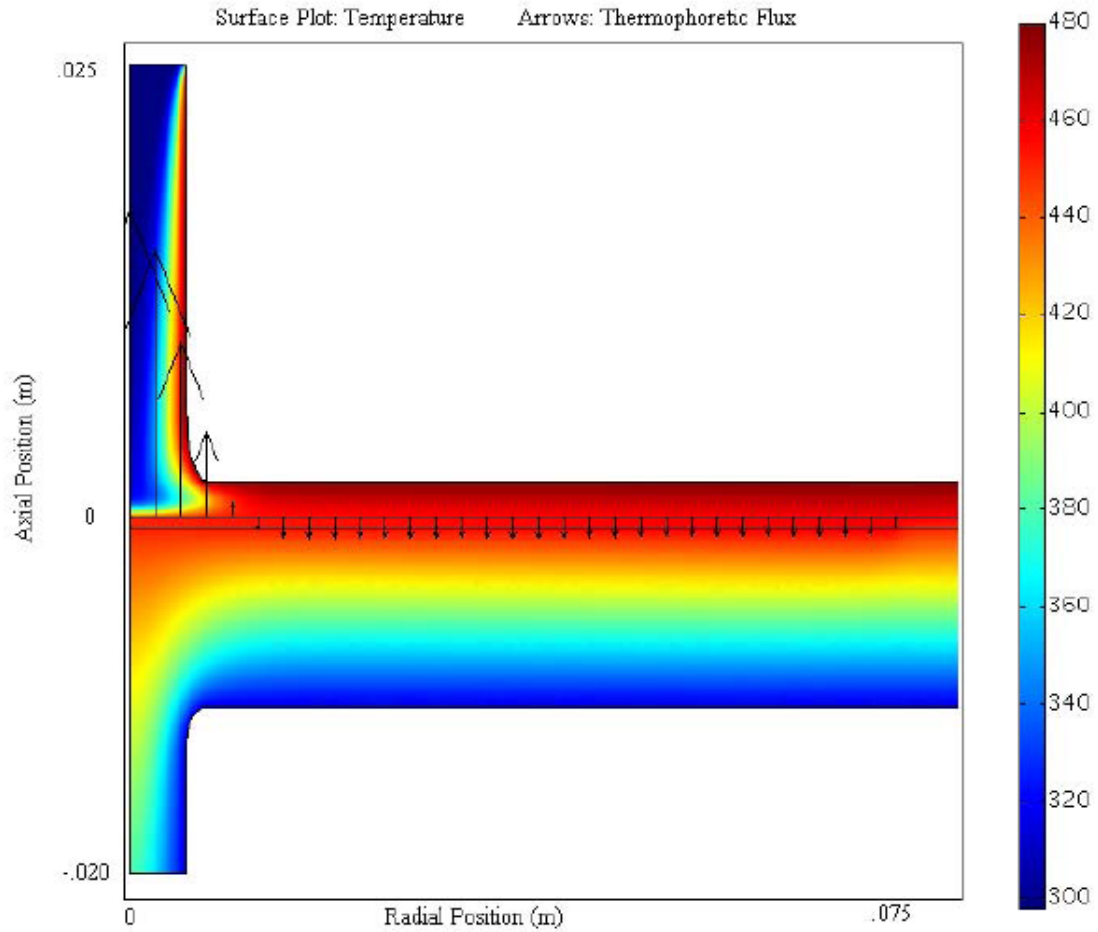


Figure A3.16. Particle Deposition without Inlet Heating.

Modeling in Femlab corroborates the predicted reversed temperature gradient when aerosol is not preheated.

References

1. U. Banin, Y. Cao, D. Katz, and O. Millo, *Nature*, **400**, 542, 1999.
2. M. Bruchez Jr, M. Moronne, P. Gin, S. Weiss, and A. Alivisatos, *Science*, **281**, 2013, 1998.
3. E. Klarreich, *Nature*, **413**, 450, 2001.
4. M. Han, X. Gao, J. Su, and S. Nie, *Nature Biotechnology*, **19**, 631, 2001.
5. P. Miquel, and J. Katz, *Journal of Material Research*, **9**, 746, 1994.
6. M. Glikin, *Theoretical Foundations of Chemical Engineering*, **30**, 390, 1996.
7. M. Glikin, D. Kutakova, and I. Glikina, *Adsorption Science and Technology*, **19**, 101, 2001.
8. R. Houriet, R. Vacassy, and H. Hofmann, *NanoStructured Materials*, **11**, 1155, 1999.
9. M. Glikin, D. Kutakova, and E. Prin, *Chemical Engineering Science*, **54**, 4337, 1999.
10. T. Johannessen, J. Jensen, M. Mosleh, J. Johansen, U. Quaade, and H. Livbjerg, *Chemical Engineering Research and Design*, **82**, 1444, 2004.
11. M. Glikin, I. Glikina, and E. Kauffeldt, *Adsorption Science and Technology*, **23**, 135, 2005.
12. W. Teoh, L. Mädler, D. Beydoun, S. Pratsinis, and R. Amal, *Chemical Engineering Science*, **60**, 5852, 2005.
13. J. Liqiang, W. Baiqi, X. Baifu, L. Shudan, S. Keying, C. Weimin, and F. Honggang, *Journal of Solid State Chemistry*, **177**, 4221, 2004.
14. H. Bai, C. Chen, C. Lin, W. Den, and C. Changs, *Industrial and Engineering Chemical Research*, **43**, 7200, 2004.
15. S. Coe, W. Woo, M. Bawendi, Bulovi, and V. cacute, *Nature*, **420**, 800, 2002.

16. M. Gao, J. Sun, E. Dulkeith, N. Gaponik, U. Lemmer, and J. Feldmann, *Langmuir*, **18**, 4098, 2002.
17. V. Colvin, M. Schlamp, and A. Alivisatos, *Nature*, **370**, 354, 1994.
18. R. Walters, G. Bourianoff, and H. Atwater, *Luminescence*, **600**, 700, 2005.
19. S. Kershaw, M. Harrison, A. Rogach, and A. Kornowski, *IEEE Journal of Selected Topics in Quantum Electronics*, **6**, 534, 2000.
20. A. Malko, A. Mikhailovsky, M. Petruska, J. Hollingsworth, H. Htoon, M. Bawendi, and V. Klimov, *Applied Physics Letters*, **81**, 1303, 2002.
21. R. Walters, P. Kik, J. Casperson, H. Atwater, R. Lindstedt, M. Giorgi, and G. Bourianoff, *Applied Physics Letters*, **85**, 2622, 2004.
22. D. Klein, R. Roth, A. Lim, A. Alivisatos, and P. McEuen, *Nature*, **389**, 699, 1997.
23. J. Holmes, K. Ziegler, R. Doty, L. Pell, K. Johnston, and B. Korgel, *Journal of the American Chemical Society*, **123**, 3743, 2001.
24. L. Pell, A. Schricker, F. Mikulec, and B. Korgel, *Langmuir*, **20**, 6546, 2004.
25. P. Shah, T. Hanrath, K. Johnston, and B. Korgel, *Journal of Physical Chemistry B*, **108**, 9574, 2004.
26. D. English, L. Pell, Z. Yu, P. Barbara, and B. Korgel, *Nano Letters*, **2**, 681, 2002.
27. S. Tiwari, F. Rana, H. Hanafi, A. Hartstein, E. Crabbe, and K. Chan, *Applied Physics Letters*, **68**, 1377, 1996.
28. T. Feng, H. Yu, M. Dicken, J. Heath, and H. Atwater, *Applied Physics Letters*, **86**, 033103, 2005.
29. M. Brongersma, A. Polman, K. Min, and H. Atwater, *Journal of Applied Physics*, **86**, 759, 1999.

30. M. Ostraat, J. De Blauwe, M. Green, L. Bell, H. Atwater, and R. Flagan, *Journal of the Electrochemical Society*, **148**, G265, 2001.
31. M. Ostraat, J. De Blauwe, M. Green, L. Bell, M. Brongersma, J. Casperson, R. Flagan, and H. Atwater, *Applied Physics Letters*, **79**, 433, 2001.
32. H. Rumpf, K. Sommer, and K. Steier, *International Chemical Engineering*, **18**, 1978.
33. H. Rumpf, K. Sommer, and K. Steier, *Chemie Ingenieur Technik*, **48**, 300, 1976.
34. D. Phares, G. Smedley, and R. Flagan, *Journal of Aerosol Science*, **31**, 1335, 2000.
35. G. Smedley, D. Phares, and R. Flagan, *Experiments in Fluids*, **26**, 324, 1999.
36. G. Smedley, D. Phares, and R. Flagan, *Experiments in Fluids*, **26**, 116, 1999.
37. G. Ulrich, *Chemical Engineering News*, **62**, 22, 1984.
38. S. Pratsinis, *Progress in Energy and Combustion Science*, **24**, 197, 1998.
39. W. Stark, and S. Pratsinis, *Powder technology*, **126**, 103, 2002.
40. R. Mueller, L. Mädler, and S. Pratsinis, *Chemical Engineering Science*, **58**, 1969, 2003.
41. W. R. Cannon, S. C. Danforth, J. S. Haggerty, and R. A. Marra, *American Ceramic Society Bulletin*, **59**, 1980.
42. W. R. Cannon, S. C. Danforth, J. H. Flint, K. S. Lai, and J. S. Haggerty, *American Ceramic Society Bulletin*, **58**, 1979.
43. H. Branz, L. Liem, C. Harris, S. Fan, J. Flint, D. Adler, and J. Haggerty, *Solar cells*, **21**, 177, 1987.
44. U. Kortshagen, U. Bhandarkar, M. Swihart, and S. Girshick, *Pure and Applied Chemistry*, **71**, 1871, 1999.
45. N. Rao, S. Girshick, J. Heberlein, P. McMurry, S. Jones, D. Hansen, and B. Micheel, *Plasma Chemistry and Plasma Processing*, **15**, 581, 1995.

46. D. Holunga, R. Flagan, and H. Atwater, *Industrial and Engineering Chemical Research*, **44**, 6332, 2005.
47. R. Bird, W. Stewart, and E. Lightfoot, *Transport Phenomena* (John Wiley and Sons, New York, New York, ed. 1st, 1960).
48. R. Flagan, and M. Lunden, *Materials Science and Engineering. A, Structural Materials: Properties, Microstructure and Processing*, **204**, 113, 1995.
49. R. C. Flagan, and J. H. Seinfeld, *Fundamentals of Air Pollution Engineering*. (Prentice Hall, Englewood Cliffs, NJ, 1998).
50. S. Corrsin, *AIChE Journal*, **3**, 329, 1957.
51. S. Zhang, Y. Akutsu, L. Russell, R. Flagan, and J. Seinfeld, *Aerosol Science and Technology*, **23**, 357, 1995.
52. S. Zhang, and R. Flagan, *Journal of Aerosol Science*, **27**, 1179, 1996.
53. R. P. Camata, H. A. Atwater, and R. C. Flagan, *Journal of Aerosol Science*, **32**, 583, 2001.
54. D. Collins, R. Flagan, and J. Seinfeld, *Aerosol Science and Technology*, **36**, 1, 2002.
55. R. Flagan, *Aerosol Science and Technology*, **30**, 556, 1999.